Importance of pyrolysis and catalytic decomposition for the direct utilization of methanol in solid oxide fuel cells

Massimiliano Cimenti, Josephine M. Hill*

Department of Chemical and Petroleum Engineering, Schulich School of Engineering, University of Calgary, 2500 University Drive NW, Calgary, AB T2N 1N4, Canada

ABSTRACT

There is interest in developing solid oxide fuel cells (SOFC) operated directly with liquid fuels such as methanol. This mode of operation increases the complexity of the anodic processes, since thermal and catalytic decomposition reactions are relevant. In this study, the pyrolysis and catalytic decomposition of methanol are investigated experimentally for conditions typical of SOFC. The results are compared to the thermodynamic equilibrium values and also to the predictions of a kinetics model. The main species of the thermal decomposition of methanol are H_2, CO, and HCHO; soot formation is relevant below 973 K. The presence of a catalyst allows the gas-phase composition to reach equilibrium. However, the catalysts tested – Ni/YSZ, Ni/CeO$_2$, Cu/CeO$_2$ and Cu–Co/CeO$_2$ – deactivate by coking so that the gas-phase composition reverts to that of pyrolysis alone. The results presented reveal part of the complex dynamics occurring within the anode compartment during the direct utilization of methanol.

© 2009 Elsevier B.V. All rights reserved.

1. Introduction

Fuel cells are efficient and clean electrochemical devices that convert the chemical energy of a fuel into electricity. Solid oxide fuel cells (SOFC) operate at high temperatures (i.e., 973–1273 K) and are typically composed of yttria-stabilized zirconia (YSZ) electrolytes, strontium-doped lanthanum manganite cathodes, and nickel (Ni)/YSZ anodes. Hydrogen or reformed natural gas are the preferred fuels for SOFC stationary applications [1]. However, several investigations have addressed the direct utilization of natural gas, gasoline, and other hydrocarbon fuels [2,3] in SOFC both for stationary and portable applications [4]. In the case of portable applications, the direct utilization of a liquid fuel is particularly convenient because of the reduction in size, complexity, and cost of the SOFC system [1]. Among all alternative fuels, methanol (MeOH) has been suggested as the optimal 'energy-vector' [5], and could be a potential fuel in portable SOFC. In particular, commercial grade MeOH fuel has a very low content of impurities and is oxygenated, which significantly reduces the risks of poisoning and may reduce carbon deposition if used in SOFC. Unfortunately, the exposure of Ni/YSZ anodes to fuels other than hydrogen can lead to rapid deactivation by coking [1], which can cause irreversible delamination of the anode [6].

At open circuit potential (OCP) there is no net flow of oxygen ions (O^{2-}) to the anode, and carbon deposition is expected [7]. A general distinction is made between the carbon originating in the gas-phase (pyrolytic carbon or soot) and that deposited with the intervention of a catalytic surface (catalytic carbon). Soot formation has been studied in relation to combustion reactions, while coking of metals has been extensively studied in relation to the process of natural gas reforming [8–12]. The morphology and stability of carbon deposits depends on many factors including temperature [13], anodic polarization [14] and type of feed [13,15]. Understanding the mechanism of carbon formation is another important factor in the study of direct utilization SOFC.

The processes expected to occur within the anodic compartment of a SOFC operated directly with MeOH are: (1) MeOH pyrolysis in the flow channels and anode pores; (2) MeOH catalytic decomposition on the conductive layer of the anode; (3) partial or complete electrochemical oxidation of pyrolytic and catalytic decomposition products, and potentially also of MeOH, in the functional layer of the anode; (4) steam and dry reforming of MeOH; (5) water–gas shift reaction; (6) carbon deposition and, possibly, carbon removal. Steam reforming, water–gas shift reaction, and carbon removal occur only when enough current is produced. A few studies have been published on gas-phase kinetics for SOFC [16–22]. In these studies, complex kinetics models for the pyrolysis and oxidation derived from combustion theory were used to predict the gas-phase composition in SOFC fuelled directly with methane [16], n-butane [17], jet fuel [19], n-hexane [20], butane and ethanol [21].

Currently, there are no publications on the pyrolysis and catalytic decomposition of MeOH in SOFC. All of the reactions listed above will influence the gas-phase composition in the vicinity of the electrochemically active area of the anode (functional layer), but

* Corresponding author. Tel.: +1 403 210 9488; fax: +1 403 284 4852.
E-mail address: jhill@ucalgary.ca (J.M. Hill).

the contributions of each of these processes on the overall performance of the SOFC at different operating conditions (temperature, flow rate, current density, etc.) is yet to be determined. In addition, a sufficient understanding of the gas-phase composition in the proximity of the functional layer is required in order to properly interpret electrochemical oxidation rates obtained with pure MeOH.

Thus, this study was undertaken to identify the importance of gas-phase (i.e., pyrolysis) and catalytic reactions when operating a SOFC directly on MeOH under various conditions. The contributions of pyrolysis and catalytic decomposition were separated by performing experiments in two different reactor set-ups. Pyrolysis experiments were performed in a plug-flow reactor with a blank YSZ disc while the catalytic decomposition studies were performed in a differential reactor with Ni/YSZ and metal/ceria impregnated on YSZ (where the metal is Ni, Cu, and Cu–Co) catalysts that had the same composition and microstructure as SOFC anodes. The metal/ceria catalysts have been considered as alternative anode materials for the direct utilization of hydrocarbons [23] due to their resistance to coking [24,25]. The results were compared to the thermodynamic equilibrium values and also to the compositions predicted using a kinetics model.

2. Experimental and simulation

Experiments and simulations have been combined to better understand how MeOH reacts in the anode of a SOFC. Thermodynamic calculations were carried out to predict the equilibrium composition, while MeOH pyrolysis simulations were performed using a kinetics model for an ideal plug-flow reactor of identical geometry and conditions as in the reactor used for the pyrolysis experiments. The following sections describe how the experiments and simulations were done.

2.1. Methanol pyrolysis

The pyrolysis of MeOH was tested experimentally at different temperatures and inlet flow rates in a plug-flow reactor made from a quartz tube 35 cm in length and 6.8 mm in diameter (internal). The reactor was placed inside a tubular furnace and connected to the inlet and outlet lines of an experimental set-up described elsewhere [26]. The reactor was then heated to the set-point temperature in flowing He. Once the temperature stabilized the reactor was isothermal with a characteristic temperature profile for each set-point. At steady-state the inlet feed was switched to a stream of He saturated with pure MeOH obtained using a thermostatic bubbler (301 K). The inlet composition was *ca.* 23 vol% MeOH. The outlet from the reactor was directed to a microGC (mGC3000, Agilent Tech., Santa Clara, USA) with three modules (*MolSieve 5A* 10 m × 0.32 mm with Ar carrier; *PLOT U* 8 m × 0.32 mm with He carrier; *OV1* 14 m × 0.32 mm with He carrier) and TCD detectors. The microGC was calibrated for the quantification of the following species: *MolSieve* – He, H_2, O_2, N_2, CH_4, CO; *PLOT U* – CO_2, C_2H_2, C_2H_4, C_2H_6, HCHO, H_2O; and *OV1* – CH_3OH (MeOH).

During the calibrations a standard error of 5% was estimated for H_2O, HCHO, and MeOH, while for all other species the standard error was less than 2%. The steady-state gas/vapor composition was monitored for each run over a period of 3 h. Liquid condensate was collected in a cold trap (200 K) and analyzed using a GC–MS (5975B-6890N, Agilent Tech.). The composition of the non-condensable species after the cold trap was determined for a few runs, and the mass balance was verified. The elemental balances were satisfied within an error of 5%. To characterize soot deposition, a YSZ disc (6 mm diameter) was placed at the center of the quartz tube and exposed to MeOH for 20 h for each temperature set-point. After testing, the sample was weighed and divided. A fraction of the sample was analyzed under a scanning-electron microscope and X-ray dispersive analysis (SEM-EDAX). The acceleration voltage and working distance used for SEM imaging was 25 kV and 8 mm, respectively. Another fraction of the sample was characterized with temperature programmed oxidation (TPO) by heating to 1173 K at 10 K min⁻¹ in 10% O_2 in He while monitoring the composition of the gas stream with a mass spectrometer (Cyrrus) [14].

The thermodynamic equilibrium gas-phase compositions for the decomposition of MeOH at temperatures between 925 K and 1125 K were calculated using the software CEA-NASA.[1] The calculation procedure implemented in CEA is known as non-stoichiometric formulation [27]; using this procedure it is not necessary to assume any pathways of MeOH decomposition [7]. That is, rather than using specific reaction pathways, the overall energy of the mixture is minimized as a function of the concentrations.

The pyrolysis of MeOH has been studied in relation to alcohol combustion processes, and several kinetics mechanisms have been proposed. In this study, the kinetics mechanism used within the simulations is known as San Diego Mech [28,29]. This mechanism consists of 137 reactions among 30 species [30]. The sub-mechanisms of C_2H_6, C_2H_4, and C_2H_2 reactions were also included since these molecules can be formed from the reaction between methyl radicals (•CH_3) that are produced by one of the decomposition steps of methanol (i.e., $CH_3OH \rightarrow$ •$CH_3 +$ OH).

The reactor model used in the MeOH pyrolysis simulations consisted of a single ideal plug-flow reactor to mimic the experimental set-up. The numerical solutions for the simulations were obtained using the San Diego Mech kinetics mechanism with the software Reaction Engineering Lab (COMSOL Inc., Los Angeles, USA). The model input parameters (e.g., flow rates and pressure) were derived from the actual experimental conditions and from the actual geometry of the reactor used. Isothermal conditions were assumed, and the experimental temperature profiles were used as input. The temperature profiles within the reactor were measured by sliding a type-K thermocouple inside the quartz tube while flowing He for each temperature set-point (blank run). During the temperature measurements, a flow rate of He equivalent to the volumetric flow rate for the pyrolysis experiments was used. The set-point temperature for each run corresponded to the maximum of the temperature profile for the reactor. During the pyrolysis experiments the thermocouple was placed outside the quartz tube in the middle of the reactor. The actual temperature profile during the pyrolysis experiments was assumed to be equal to that measured in the blank runs.

The extent of axial dispersion was estimated at the end of each experiment to assess the validity of the plug-flow assumption. After validation, the kinetics model was used to simulate the MeOH pyrolysis as a function of space-time in order to predict the extent of the MeOH conversion for typical experimental conditions. Simulations were performed for isothermal plug-flow and CSTR reactors. Results are reported in terms of fraction conversion (X_{MeOH}), yields (Y_i), and selectivity (S_{i-j}), according to the definitions given in [31].

2.2. Methanol catalytic decomposition

Experiments were done with catalyst discs in a differential reactor to study the catalytic decomposition of MeOH over several anode materials. These experiments simulated the reactions in the conduction layer of an anode-supported SOFC. Catalyst discs made from copper/ceria (Cu/CeO_2), copper-cobalt/ceria ($Cu–Co/CeO_2$), and nickel/ceria (Ni/CeO_2) supported on a YSZ porous layer were

---

[1] Available online at www.grc.nasa.gov/WWW/CEAWeb/.

tested and their activities compared with that of Ni/YSZ, the conventional anode material. In this study, the catalysts were prepared in the same manner as SOFC anodes; thus, the same composition and microstructure as in anodes was obtained, but for the catalyst discs, cathode and current collectors were not added.

The ceria-based catalysts were prepared using a modification of an impregnation procedure [32]. First, a dense electrolyte layer was prepared by tape-casting using commercial YSZ powders (TZ-8Y, Tosoh, Japan) [33]. A porous YSZ layer was obtained by adding cornstarch (generic brand, average particle size approximately 10 μm) and graphite powder (Alfa Aesar −325 mesh) to the YSZ mixture. Green tapes of both the dense and porous electrolytes were laminated together and punched into discs 6 mm in diameter (A = 0.283 cm^2). Discs so obtained were sintered at 1773 K for 2 h with a heating rate of 2 K min^{-1}. After sintering, the thicknesses of the dense and porous layers were approximately 50 μm and 70 μm, respectively. The apparent porosity of the porous layer was estimated as 60% based on Archimedes' method.

Ceria was deposited on the porous layer using a saturated solution of $(NH_4)_2Ce(NO_3)_6$ (Alfa Aesar) in isopropyl alcohol (IPA). Discs impregnated with ceria were dried at 343 K under vacuum for 15 min and then fired at 723 K for 60 min using heating and cooling rates of 2 K min^{-1} and 5 K min^{-1}, respectively. This procedure was repeated until the weight of CeO$_2$ was equivalent to approximately 20 wt% of the porous layer.

Cu and Ni were impregnated adding saturated solutions of metal nitrate precursor in IPA. For Ni/CeO$_2$, the precursor was Ni(NO$_3$)$_2$·6H$_2$O (99.99% metal basis, Alfa Aesar), while for Cu/CeO$_2$, the precursor was Cu(NO$_3$)$_2$·3H$_2$O (99.99% metal basis, Alfa Aesar). For Cu–Co/CeO$_2$, the impregnation was done using a solution containing Cu(NO$_3$)$_2$·3H$_2$O and Co(NO$_3$)$_2$·6H$_2$O (99.99% metal basis, Alfa Aesar) in IPA. The composition of the nitrates mixture was 64.2 wt% Cu(NO$_3$)$_2$ and 35.8 wt% Co(NO$_3$)$_2$, which is equivalent to a weight ratio of 7:3 for Cu and Co [25] as reduced metals. Impregnated discs with metals were fired following the same procedure described earlier for ceria. The metal loading was equivalent to approximately 40 wt% of the porous YSZ layer. In all cases, the degree of hydration of the metal nitrates was determined by thermogravimetric analysis of the salts.

Ni-YSZ anodes were prepared from commercial powders of NiO (Alfa Aesar) and YSZ (Tosoh, TZ-8Y) by tape-casting. Surface area and particle size distribution of these powders were measured prior to use by dynamic light scattering (DLS; Malvern Mastersizer 2000) and nitrogen-physisorption (BET; Micrometrics TriStar 3000). The NiO had a unimodal particle size distribution with a peak at 15 μm, and BET surface area of 5.7 m^2 g^{-1}. The YSZ had a bi-modal particle size distribution with the main peak at 0.1 μm, and a BET surface area of 18.5 m^2 g^{-1}. A mixture of 57 wt% NiO and 43 wt% YSZ (equivalent to 50% after reduction) was used for tape-casting [33]. The NiO/YSZ green tape was punched into discs 6 mm in diameter. Discs were sintered for 2 h at 1623 K using a heating rate of 2 K min^{-1}. After sintering, the thickness of the NiO/YSZ discs was approximately 70 μm. Ni reduction was performed *in-situ*.

The prepared catalyst discs were placed in a quartz tube, 9 mm in diameter, with two quartz rods that reduced the gas-phase volume, such that this reactor behaved as a differential reactor. The catalyst discs were held in place by quartz wool. The gas-phase (empty volume) in the middle of the tube, where the temperature is uniform, was approximately 1.2 cm^3. The reactor was heated to 1073 K in 10 vol% H$_2$ for at least 2 h to achieve complete reduction of the catalysts. The flow was switched to pure He for *ca.* 15 min, and then to a MeOH–He mixture, obtained by flowing He at 25 mL min^{-1} (STP) through pure MeOH. The estimated residence time in the hot zone (1073 K) was approximately 3 s. These conditions were selected to minimize the MeOH conversion due to pyrolysis. The gas-phase composition of the outlet stream was monitored with a microGC for a period of 12 h, after which the reactor was cooled down in pure He. The catalytic decomposition experiments were run in duplicate for each anode material and also run with a blank YSZ disc. The tested catalysts were then analyzed by visual inspection, by TPO, and by SEM/EDAX.

The catalyst deactivation was estimated from the difference between the MeOH fraction conversion with and without catalyst (i.e., $\Delta X = X_{CD} - X_{TD}$, where X_{CD} is the conversion with catalyst and X_{TD} is the steady-state conversion by pyrolysis only, as measured in the blank run). The catalyst activity $a(t)$ is defined as the ratio of the rate of decomposition after time t to the rate of decomposition over the fresh catalyst. The kinetics of catalytic decomposition was fit to the empirical relationships proposed in [31].

3. Results and discussion

3.1. Methanol pyrolysis

The calculated thermodynamic equilibrium composition for the gas-phase decomposition of 25 vol% MeOH in He as a function of temperature is shown in Fig. 1. The predicted MeOH conversion is 100% over the entire temperature range (923–1123 K) and the only stable species at equilibrium are H$_2$, CO, CH$_4$, C (graphite), and H$_2$O. Above 1023 K, the main products are H$_2$ and CO, with a ratio approaching 2. Species such as HCHO, C$_2$H$_2$, C$_2$H$_4$ and C$_2$H$_6$ are not predicted.

The results of the pyrolysis experiments are shown by the symbols in Figs. 2–4. For these experiments, the inlet feed was a mixture of MeOH (*ca.* 23 vol%) in He delivered at flow rates between 1×10^{-6} mol s^{-1} and 10×10^{-6} mol s^{-1}. Each point in Fig. 2 represents the average of 12 measurements repeated over 3 h after isothermal steady-state conditions were reached. The standard error was smaller than 1% for all species. The main species detected for the pyrolysis of MeOH were H$_2$, CO and HCHO with trace amounts (<0.5 vol%) of CH$_4$, H$_2$O, C$_2$H$_2$, and C$_2$H$_4$. The liquid condensate collected in the cold trap was composed mostly of MeOH, HCHO, and polymerized HCHO (trioxane). The composition measured during the pyrolysis experiments was significantly different from the equilibrium predictions for temperatures lower than 1123 K. As shown in Fig. 2, the decomposition of MeOH did not start until 973 K, indicating that the reactions were kinetically limited. The first species detected were H$_2$ and HCHO. Only at 1123 K, did all the MeOH decompose to H$_2$ and CO, as predicted by the equilibrium calculations. Furthermore, species such as CH$_4$ and H$_2$O were detected only in trace amounts, and HCHO was an intermediate.
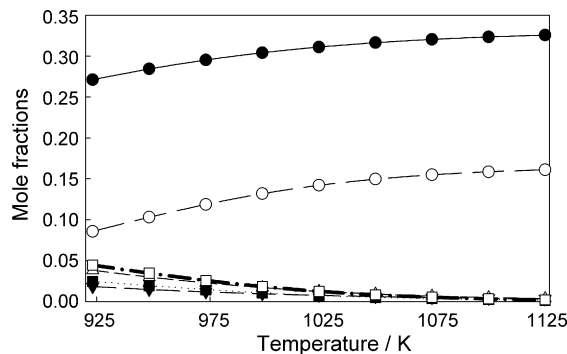

Fig. 1. Calculated thermodynamic equilibrium composition as a function of temperature for MeOH pyrolysis. The species are (●) H$_2$, (○) CO, (▼) CO$_2$, (△) CH$_4$, (■) H$_2$O, and (□) C (graphite).
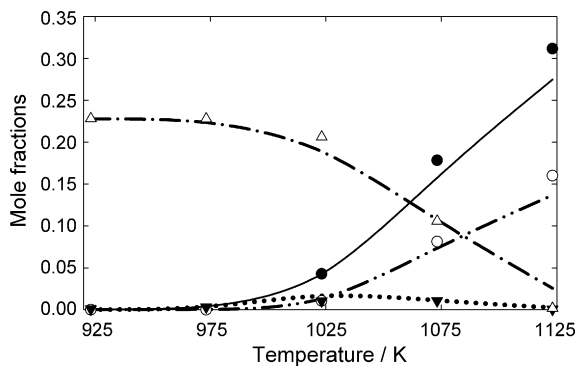
Fig. 2. Experimental (symbols) and simulated (lines) compositions at the reactor outlet for the pyrolysis of MeOH as a function of temperature (inlet molar rate 2.5×10^{-5} mol s^{-1}). The species are: H_2 (●, solid line), MeOH (△, dash-dot line), CO (○, dash-dot-dot line), HCHO (▼, dotted line).
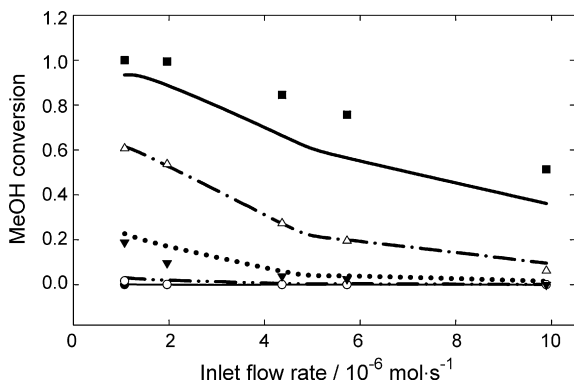

Fig. 3. Experimental (symbols) and simulated (lines) MeOH fractional conversion as a function of space time at 1123 K (■, solid line), 1073 K (△, dash-dot line), 1023 K (▼, dotted line), and 973 K (○, dash-dot-dot line).
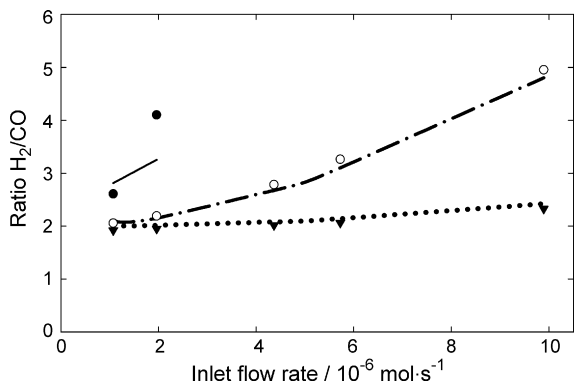

Fig. 4. Experimental (symbols) and simulated (lines) H_2/CO ratio as a function of the inlet flow rate at 1123 K (▼, dotted line), 1073 K (○, dash-dot line), and 1023 K (●, solid line).

The conditions of the pyrolysis experiments were simulated with the San Diego Mech kinetics mechanism. The lines in Fig. 2, and also in Figs. 3 and 4, represent the results of the simulation, which are in good agreement with the experiments, except at 1123 K, at which the model predicts that approximately 2 mol% MeOH will be present. Accordingly, the calculated concentrations of H_2 and CO are 10% and 15%, respectively, lower than the measured values.

Pyrolytic carbon (soot) was observed along the quartz tube for most of the experiments. The deposits were typically found anywhere in the reactor where the temperature was between 773 K

and 973 K.[2] For the runs with set-point temperatures of 1073 K or higher, the central area of the tube was relatively clean, as predicted at equilibrium (see Fig. 1).

The fraction conversion of MeOH as a function of the molar flow rate is shown in Fig. 3. As the flow rate increased, the conversion of MeOH decreased due to the shorter residence time in the reactor. The calculated conversion is in good agreement with the experimental results, except again at 1123 K for which the simulated conversion is lower than the observed conversion. The ratios of H_2 to CO as a function of flow rate for different temperatures are shown in Fig. 4. For low flow rates ($<2 \times 10^{-6}$ mol s^{-1}) and high temperatures (>1073 K) the ratio is approximately 2, as expected from the thermodynamic analysis [7]. The calculated selectivity is in very good agreement with the experimental results. The ratios at temperatures lower than 1023 K are not shown because CO was not detected.

In general, the San Diego Mech kinetics mechanism implemented with a plug-flow reactor model accurately predicted the majority of the experimental results. The significant differences observed between simulations and experiments for the runs at 1123 K are likely due to the inaccuracies in the measurement of the temperature profile, to deviations from ideal flow conditions, or to inadequacy of the kinetic model at the higher temperatures. The sensitivity analysis of the model indicated that a temperature variation of ±5 K at 1123 K can result in a variation of 7% for the final MeOH concentration. The experimental error in the measurement of the temperature profile is likely to be the main cause of the deviations observed for the runs at 1123 K, as these runs had the highest temperature gradient and the actual temperature could have been significantly perturbed by the insertions of the thermocouple inside the reactor during calibration.

To verify that the hypothesis of ideal plug-flow reactor is reasonable, we compared simulation results obtained using the plug-flow model and using the axial dispersion model (with closed boundary [34]) for the temperature range considered. In the case of axial dispersion, the diffusivity of the multi-component gas mixture was estimated using an approximation of the Maxwell–Stefan equation [35], and the binary diffusivity coefficients were estimated using the Chapman–Enskog and the Brokaw equations for the non-polar species and polar species, respectively [36]. According to the results obtained, longitudinal mixing caused by axial dispersion should be negligible at isothermal conditions with uniform temperature profiles at temperatures below 923 K. However, longitudinal mixing is likely to increase when there is a steep temperature profile along the reactor as a consequence of longitudinal thermal gradients, variations of the gas velocity, and density variations. These factors all increase the axial dispersion coefficient, and as a result, the ideal plug-flow reactor model is not adequate to simulate the pyrolysis of MeOH for higher temperatures unless mass transfer processes are also included in the simulation.

Another limitation of the model used is that it does not include cyclic and aromatic species, thus it cannot predict the formation of soot. In other more detailed kinetics models [16,21] the propensity for carbon formation in the anode channels was related to the rate of formation of cyclic hydrocarbon species, assuming that a fraction of these species will eventually condense. As the main purpose of this work was to predict the gas-phase composition in the proximity of the functional layer, we adopted the simplified approach proposed in Refs. [28,37].

---

[2] The set-point temperature for each experiment corresponded to the maximum of the temperature profile along the reactor tube.

3.2. Methanol catalytic decomposition

The second part of this study investigated the contribution from catalytic reactions, over different catalysts, on the gas-phase composition. The gas-phase was analyzed after flowing MeOH through a differential reactor in which the gas-phase in the hot zone of the reactor was limited to minimize pyrolysis. Initially a blank run was done to determine the level of pyrolysis reactions. The average steady-state MeOH conversion and product composition for the blank run, as indicated by larger symbols in Fig. 1, are consistent with the simulation results obtained using the San Diego Mech kinetics mechanism for the same conditions (i.e., 16.8 vol% MeOH). Therefore, the conversion obtained for the blank run is attributed to only pyrolysis and not to any reactions on the YSZ pellet.

The outlet gas composition profiles were similar for all the catalysts tested and the profile for Cu/CeO$_2$ exposed to MeOH at 1073 K is shown in Fig. 5. The concentrations of H$_2$ and CO decreased over a period of 12 h from initial values close to the equilibrium composition (i.e., 32 vol% H$_2$ and 15.4 vol% CO) to the steady-state values obtained in the blank run. Simultaneously, the concentrations of HCHO and MeOH increased to the blank run values as the catalysts deactivated.

The deactivation profiles of the catalysts are shown in Fig. 6. Experimental data were fit to semi-empirical expressions proposed to describe the changes of catalyst activity as a result of fouling [31]. The deactivation profiles of the Cu/CeO$_2$ and Cu–Co/CeO$_2$ catalysts fit similar exponential deactivation curves [31]. In contrast, the Ni/CeO$_2$ catalyst deactivated more gradually and its profile fit a sigmoid-shaped deactivation curve [31]. The deactivation profile of the Ni/YSZ catalyst also fit a sigmoid curve, although the activity was maintained for a much shorter time than for the Ni/CeO$_2$ catalyst. The Cu–Co/CeO$_2$ catalyst showed the slowest apparent rate of deactivation and was still active after 12 h on stream.

The different deactivation profiles could be indicative of different mechanisms of deactivation [31]. For an exponential decay, the deactivation may be caused simply by fouling of the catalyst surface. For a sigmoidal decay, the process of deactivation is likely more complex, and may involve a modification of the catalyst (Ni) surface in parallel to fouling [38,39]. A deeper investigation of the carbon formation mechanism, which is beyond the scope of this study, is required [40] to fully understand the deactivation process.

These results are indicative of the general concentration and catalyst deactivation profiles for MeOH decomposition in an SOFC anode compartment at OCP (i.e., with no O^{2-} ion flux). Pyrolysis by itself resulted in a gas-phase composition (blank run values in Fig. 5) that was far from equilibrium. With a catalytic surface present, the gas-phase composition reached the equilibrium
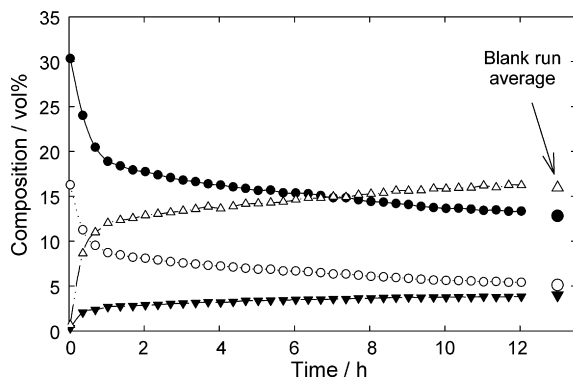
Fig. 6. Catalyst activity as a function of time for Cu/CeO$_2$ (□), Cu–Co/CeO$_2$ (○), Ni/CeO$_2$ (◊), and Ni/YSZ (▽) exposed to MeOH at 1073 K. The data for the Cu/CeO$_2$ and Cu–Co/CeO$_2$ catalysts were fit to an exponential decay curve while those for the Ni/CeO$_2$ and Ni/YSZ catalysts were fit to a sigmoidal decay curve.

composition initially but then, as the catalyst deactivated, the composition approached that achieved by pyrolysis alone (i.e., catalytic decomposition became negligible).

3.3. Carbon deposition

The carbon deposited on the discs during the experiments was analyzed by SEM and by TPO. After 12 h of exposure to MeOH at 1073 K, all of the discs (YSZ blank and catalysts) had varying amounts of visible catalytic carbon and/or soot on their surfaces. The least amount of carbon was on the blank disc and the most amount of carbon was on the Ni-containing catalysts. As has been seen previously with Ni/YSZ exposed to methane [13,41], the Ni/YSZ disc was warped and fractured after exposure to MeOH, while the other discs were still flat and compact.

Fig. 5. Outlet composition as a function of time for the Cu/CeO$_2$ catalyst exposed to MeOH at 1073 K. The species are: H$_2$ (●), CO (○), HCHO (▼), and MeOH (△). The symbols on the right are the steady-state compositions for MeOH pyrolysis measured in a blank run.
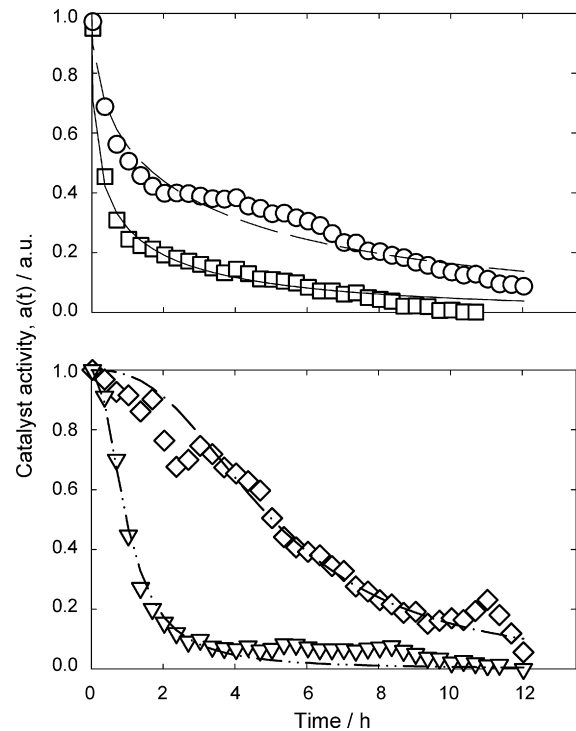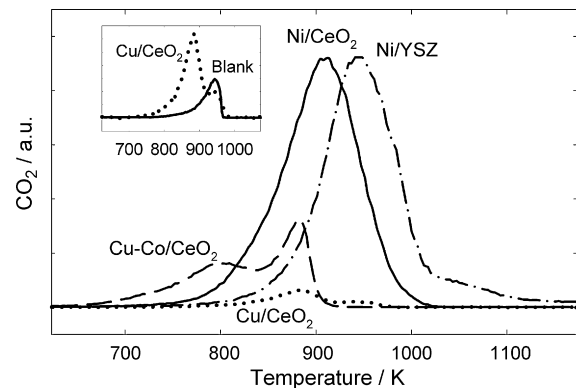
Fig. 7. TPO profiles for Ni/YSZ (dash-dot line), Ni–CeO$_2$ (solid line), Cu/CeO$_2$ (dotted line), and Cu–Co/CeO$_2$ (dashed line) catalysts exposed to MeOH at 1073 K for 12 h. The insert is the TPO for Cu/CeO$_2$ and the blank YSZ disc.
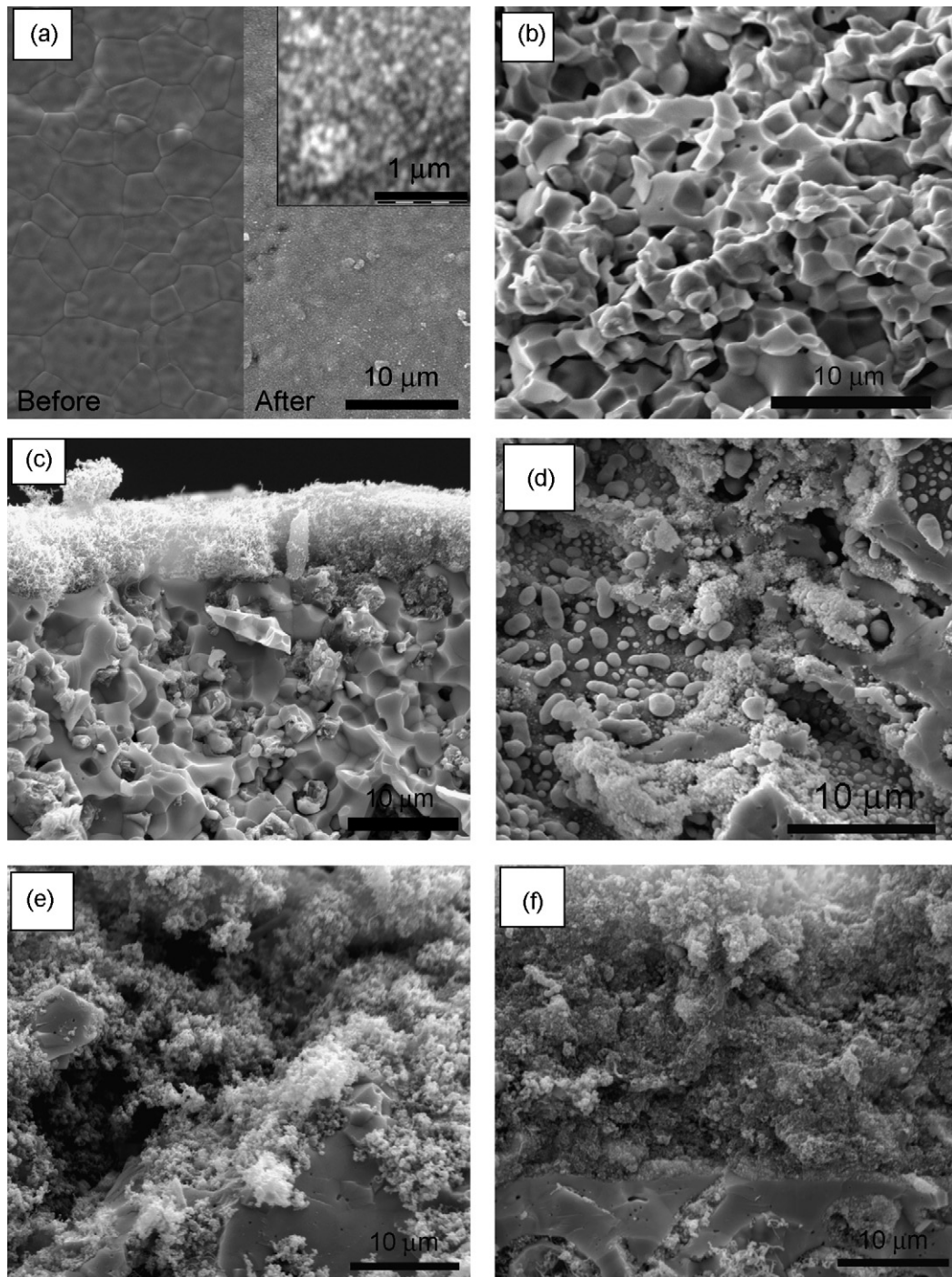
Fig. 8. SEM micrographs of (a) surface of YSZ disc before and after exposure to MeOH, and cross-sections of (b) as-prepared Ni/YSZ, (c) used Ni/YSZ, (d) as-prepared Cu/CeO$_2$, (e) used Cu–Co/CeO$_2$, and (f) used Ni/CeO$_2$. All used catalysts were exposed to MeOH at 1073 K for 12 h.

The TPO results shown in Fig. 7 are only qualitative because of the difficulty in recovering all of the catalyst and carbon material from the reactor. The TPO profile for the YSZ disc had one peak temperature around 940 K. The amount of carbon deposited on the blank sample was significantly smaller than that deposited on the catalyst discs; consequently, the amount of pyrolytic carbon deposited over the catalysts was negligible.

The TPO profiles for the Cu/CeO$_2$ and Cu–Co/CeO$_2$ catalysts each had two peaks at 873 K and 930 K, and 825 K and 890 K, respectively. The TPO profiles of the Ni/CeO$_2$ and Ni/YSZ catalysts had single peaks at 908 K and 953 K, respectively. The higher peak temperatures for the Ni catalysts indicates that the carbon was less

reactive and more difficult to remove from these catalyst. No peaks for H$_2$O were observed during the TPO analysis, indicating that the deposited carbon in these samples contained a negligible amount of hydrogen. It was expected that more carbon would be deposited on the Ni catalysts than on the Cu and Cu–Co catalysts [10]. Although the amount of carbon is comparable on the Ni/CeO$_2$ and Ni/YSZ catalysts, the Ni is more highly dispersed on the former catalyst and so there were more sites for carbon formation. The amount of carbon deposited could not be quantified and/or normalized by the amount of Ni in each catalyst because of the difficulty in transferring the samples from the differential reactor to the TPO analysis cells.

The Ni/CeO$_2$ catalyst maintained its activity longer than the Ni/YSZ catalyst (Fig. 6) although both catalysts appeared severely coked. Similarly, the Cu–Co/CeO$_2$ catalyst maintained its activity longer than the Cu/CeO$_2$ catalyst (Fig. 6) even though more carbon was deposited on the former catalyst. The amount of carbon deposited on a catalyst often does not directly correlate with the activity of the catalyst because the carbon can move off the active site onto the support [10]; thus, the interaction of the carbon with the catalyst is important.

The microstructures of the catalysts were observed by SEM before and after exposure to MeOH. The soot deposits on the YSZ blank disc were visible as *ca.* 100 nm particles on the surface (Fig. 8a). Images of the as-prepared Ni/YSZ and Cu/CeO$_2$ catalysts are shown in Fig. 8b and d, respectively. Fig. 8b is also representative of the reduced Cu–Co/CeO$_2$ and Ni/CeO$_2$ catalysts. The morphology of the Ni/YSZ and metal/ceria catalysts is quite different and reflects the different preparation methods used. Both the morphology and the presence of ceria may have influenced the type of carbon deposited after exposure to MeOH. The Ni/YSZ disc (Fig. 8c) contained numerous carbon filaments on the surface (diameter 50–100 nm) and swollen Ni particles within the bulk, which significantly reduced the porosity.

In contrast, only a few carbon fibers were visible in the pores of the Cu/CeO$_2$ catalyst (not shown), and significantly less carbon was deposited than on the other catalysts. Even though little carbon was evident, the Cu/CeO$_2$ catalysts lost almost all catalytic activity for MeOH decomposition. The deactivation of the Cu/CeO$_2$ catalyst could have been caused also by Cu and CeO$_2$ sintering as reported elsewhere [42]. The carbon deposits on the Cu–Co/CeO$_2$ and Ni/CeO$_2$ catalysts had similar morphologies but there was significantly more carbon on Ni/CeO$_2$ (Fig. 8e and f). Almost no porosity remained in the Ni/CeO$_2$ structure and thus, diffusion resistance, as well as the blockage of active sites, may have contributed to the loss of activity. As has been observed when Ni/YSZ catalysts were exposed to methane [13], the presence of CeO$_2$ hinders the movement of carbon into the Ni structure.

4. Conclusions

The reaction of MeOH in an environment similar to that of an SOFC anode compartment has been studied. Both the pyrolysis and catalytic decomposition reactions were investigated. Because the gas-phase decomposition of MeOH is kinetically limited up to temperatures of 1123 K, the gas-phase will not reach thermodynamic equilibrium unless a catalyst is present. The catalysts tested in this study – Ni/CeO$_2$, Cu/CeO$_2$, Cu–Co/CeO$_2$ and Ni/YSZ – deactivated after several hours on stream and the gas-phase composition reverted to that obtained solely by pyrolysis reactions.

The reactor set-up can significantly influence the gas-phase composition reaching an SOFC anode. In particular, the gas-phase compositions depended on both temperature and inlet flow rate. The trends observed experimentally were generally well captured by the model developed with the San Diego Mech kinetics mechanism using a plug-flow reactor. The model predictions were not accurate above 1073 K, likely due to errors in the measurement of the temperature profile or axial dispersion not being negligible at the higher temperatures.

Although not predicted thermodynamically, carbon was formed on the catalysts exposed to MeOH at 1073 K. Relatively little soot (carbon produced by pyrolysis) was deposited and most carbon was formed catalytically on the surface. The most carbon was deposited on the catalysts containing Ni, and this carbon blocked active sites as well as the pores. Sintering may have contributed to the deactivation of the catalysts containing Cu. The shapes of the catalyst deactivation profiles were different depending on whether the catalysts contained Ni (sigmoidal decay) or Cu (exponential decay).

The results of this study are helpful for interpreting results obtained for the direct utilization of MeOH in SOFC. The reactions (gas-phase and catalytic) and resulting composition observed *ex-situ* in this study are expected to be similar to that in the SOFC anode at OCP. The catalytic activity of the conductive layer determines the gas-phase composition in the immediate proximity of the functional layer, and, in turn, the local composition at the functional layer determines the OCP or the electromotive force of the SOFC. For fuels such as MeOH, the actual composition at the anode might be quite different from the composition measured at the outlet of the cell. The composition gradients can be effectively modeled using relevant reactor and kinetics models.

References

[1] S.C. Singhal, K.E. Kendall, High Temperature Solid Oxide Fuel Cells—Fundamentals Design and Applications, 1st, Elsevier Ltd., Oxford, UK, 2003.
[2] M.D. Gross, J.M. Vohs, R.J. Gorte, J. Mater. Chem. 17 (2007) 3071–3077.
[3] G. McIntosh, Chem. Rev. 104 (2004) 4845–4865.
[4] S.C. Singhal, Solid State Ionics 152 (2002) 405–410.
[5] G.A. Olah, Chem. Eng. News 81 (2003) 5–15.
[6] T. Kim, G. Liu, M. Boaro, S.I. Lee, J.M. Vohs, R.J. Gorte, O.H. Al-Madhi, B.O. Dabbousi, J. Power Sources 155 (2006) 231.
[7] M. Cimenti, J.M. Hill, J. Power Sources 186 (2008) 377–384.
[8] C.H. Bartholomew, Catal. Rev.-Sci. Eng. 24 (1982) 67–112.
[9] C.H. Bartholomew, Chem. Eng. 91 (1984) 96–112.
[10] C.H. Bartholomew, Appl. Catal., A 212 (2001) 17–60.
[11] D.L. Trimm, Catal. Today 37 (1997) 233–238.
[12] D.L. Trimm, Catal. Today 49 (1999) 3–10.
[13] H. He, J.M. Hill, Appl. Catal., A 317 (2007) 284.
[14] V. Alzate-Restrepo, J.M. Hill, Appl. Catal., A 342 (2008) 49.
[15] N.M. Rodriguez, A. Chambers, R.T.K. Baker, Langmuir 11 (1995) 3862–3866.
[16] K.M. Walters, A.M. Dean, H.Y. Zhu, R.J. Kee, J. Power Sources 123 (2003) 182–189.
[17] C.Y. Sheng, A.M. Dean, J. Phys. Chem. A 108 (2004) 3772–3783.
[18] E.S. Hecht, G.K. Gupta, H.Y. Zhu, A.M. Dean, R.J. Kee, L. Maier, O. Deutschmann, Appl. Catal., A 295 (2005) 40–51.
[19] G.K. Gupta, E.S. Hecht, H.Y. Zhu, A.M. Dean, R.J. Kee, J. Power Sources 156 (2006) 434–447.
[20] K.L. Randolph, A.M. Dean, Phys. Chem. Chem. Phys. 9 (2007) 4245–4258.
[21] G.K. Gupta, A.M. Dean, K. Ahn, R.J. Gorte, J. Power Sources 158 (2006) 497–503.
[22] H.Y. Zhu, R.J. Kee, V.M. Janardhanan, O. Deutschmann, D.G. Goodwin, J. Electrochem. Soc. 152 (2005) A2427–A2440.
[23] R.J. Gorte, S. Park, J.M. Vohs, C.H. Wang, Adv. Mater. (Weinheim Ger.) 12 (2000) 1465–1469.
[24] A. Atkinson, S. Barnett, R.J. Gorte, J.T.S. Irvine, A.J. McEvoy, M. Mogensen, S.C. Singhal, J. Vohs, Nat. Mater. 3 (2004) 17–27.
[25] S.I. Lee, K. Ahn, J.M. Vohs, R.J. Gorte, Electrochem. Solid State Lett. 8 (2005) A48–A51.
[26] M. Cimenti, Direct utilization of methanol and ethanol in SOFC, Ph.D. Thesis, University of Calgary, Calgary, Canada, 2008.
[27] W.R. Smith, R.W. Missen, Chemical Reaction Equilibrium Analysis: Theory and Algorithms, John Wiley & Sons, New York, 1982.
[28] M.V. Petrova, F.A. Williams, Combust. Flame 144 (2006) 526–544.
[29] S.C. Li, F.A. Williams, J. Eng. Gas Turbines Power-Trans. ASME 124 (2002) 471–480.
[30] P. Saxena, Numerical and experimental studies of ethanol flames and autoignition theory for higher alkanes, Ph.D. Thesis, University of California, San Diego, 2007.
[31] H.S. Fogler, Elements of Chemical Reaction Engineering, 3rd ed., Prentice-Hall, Upper Saddle River, NJ, 1999.
[32] R.J. Gorte, H. Kim, J.M. Vohs, Novel, J. Power Sources 106 (2002) 10–15.
[33] M. Cimenti, J.M. Hill, Asia-Pacific J. Chem. Eng. 4 (2009) 45–54.
[34] C.G.J. Hill, An Introduction to Chemical Engineering Kinetics & Reactor Design, John Wiley & Sons, Inc., Hoboken, NJ, 1977.
[35] E.L. Cussler, Diffusion: Mass Transfer in Fluid Systems, 2nd ed., Cambridge University Press, New York, 1997.

[36] R.S. Brokaw, Ind. Eng. Chem. Proc. Des. Dev. 8 (1969) 240–253.
[37] F.A. Williams, Chemical-Kinetic Mechanisms for Combustion Applications, http://www-mae.ucsd.edu/~combustion/cermech/ (accessed April 2009).
[38] I.S. Nam, J.R. Kittrell, Ind. Eng. Chem. Proc. Des. Dev. 23 (1984) 237–242.
[39] A. Romero, J. Bilbao, J.R. Gonzalez-Velasco, Ind. Eng. Chem. Proc. Des. Dev. 20 (1981) 570–575.
[40] J. Corella, A. Monzon, Ind. Eng. Chem. Res. 27 (1988) 369–374.
[41] H.P. He, J.M. Vohs, R.J. Gorte, J. Power Sources 144 (2005) 135–140.
[42] T. Kim, K. Ahn, J.M. Vohs, R.J. Gorte, J. Power Sources 164 (2007) 42–48.